


The Nb₄C₃ MXenzyme Attenuates MASH by Scavenging ROS in a Mouse Model

Shuying He^{1,*}, Yuerong Lv^{1,*}, Zixian Gao^{1,*}, Liang Peng^{1,2} 

¹Department of Gastroenterology, First Affiliated Hospital of Guangzhou Medical University, Guangzhou Medical University, Guangzhou city, Guangdong Province, People's Republic of China; ²Department of Medicine, First Affiliated Hospital of Guangzhou Medical University, Guangzhou Medical University, Guangzhou city, Guangdong Province, People's Republic of China

*These authors contributed equally to this work

Correspondence: Liang Peng, Department of Gastroenterology, Department of Medicine, First Affiliated Hospital of Guangzhou Medical University, No. 151 Yanjiang West Road, Yuexiu District, Guangzhou, Guangdong, 510120, People's Republic of China, Tel/Fax +862083062090, Email wsfirefly@126.com

Objective: The incidence of metabolic dysfunction-associated steatohepatitis (MASH) is increasing because people's dietary habits are dominated by high caloric intake and sedentary lifestyles, leading to the accumulation of lipid, reactive oxygen species (ROS) and inflammation. However, treating MASH remains a challenge.

Methods: Two-dimensional (2D) niobium carbide (Nb₄C₃) MXene nanoenzymes (MXenzymes) possess both antioxidant and anti-inflammatory properties and have attracted considerable attention in the tumor and engineering fields. The Nb₄C₃ MXenzyme was developed for MASH therapy and exhibited biosafety and antilipid peroxidation activity.

Results: Nb₄C₃ reduced excessive ROS and proinflammatory cytokine levels through its antilipid peroxidation activities, resulting in the inhibition of hepatocyte lipid accumulation and inflammation in a methionine–choline-deficient diet (MCD)-induced murine MASH model. Mechanistically, Nb₄C₃ not only inhibited lipid accumulation and disrupted lipid metabolism in hepatocytes but also attenuated fatty acid-induced cell death by reducing intracellular ROS levels, which significantly promoted the polarization of M1 macrophages to M2 macrophages by alleviating oxidative stress and suppressing inflammatory factor expression.

Conclusion: The Nb₄C₃ MXenzyme can be used as a multifunctional bioactive material to alleviate hepatic steatosis and inflammation in MASH mice through its robust antioxidant and anti-inflammatory activities.

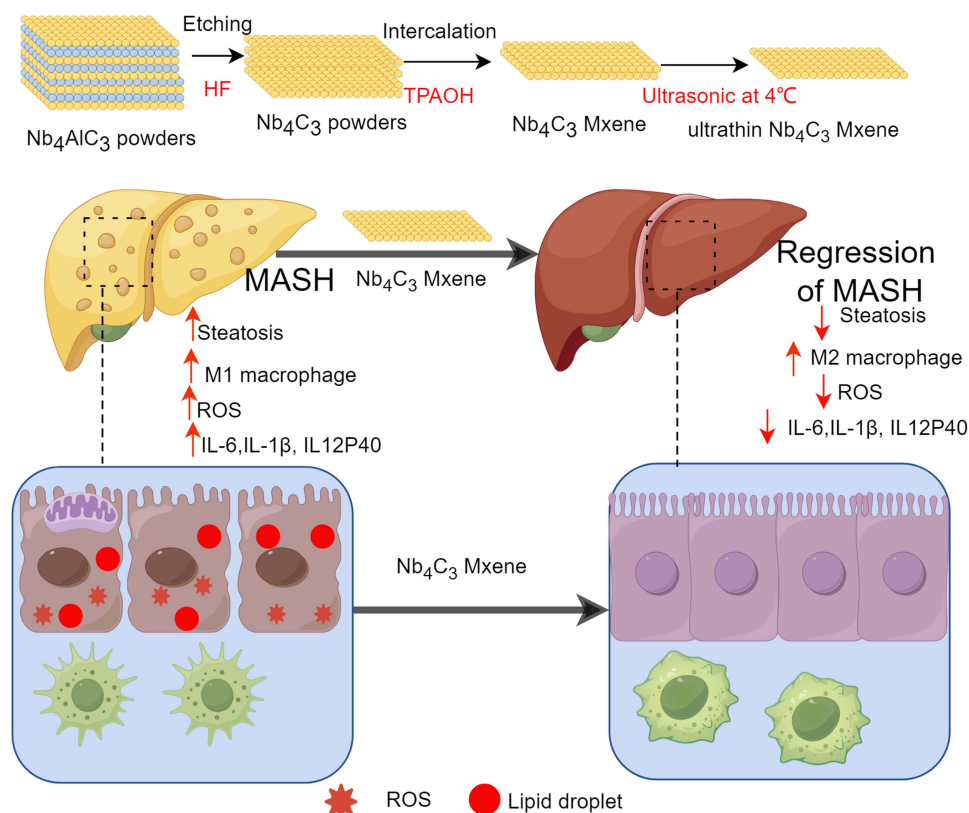
Keywords: metabolic dysfunction-associated steatohepatitis, Nb₄C₃, ROS scavenging, macrophage

Introduction

Metabolic dysfunction-associated fatty liver disease (MAFLD) includes a spectrum of liver abnormalities ranging from benign steatosis to metabolic dysfunction-associated steatohepatitis (MASH);^{1,2} these abnormalities are characterized by intrahepatic fat accumulation, macrophage activation, hepatocyte apoptosis, and fiber formation and have become the leading diseases that lead to liver-related morbidity and mortality.^{2,3} The prevalence of MAFLD has increased to 37.8%, and MAFLD affects 46.9 of 1000 individuals.⁴ Providing suitable and cost-effective therapeutic interventions in the early stages of MAFLD has become increasingly necessary to avoid MASH, cirrhosis, and cancer. Many clinical trials targeting each process have been conducted worldwide, but no approved therapeutic strategies for MASH are available.⁵

Toxic reactive oxygen species (ROS), including free radicals and nonradicals, can cause cell death or induce inflammation and fibrosis during MASH pathogenesis when the oxidant–antioxidant balance is markedly disrupted by ROS overproduction.^{6,7} ROS include free radicals such as peroxy (RO₂), alkoxyl (RO), superoxide (O²⁻), and hydroperoxyl (HO₂) and certain nonradical compounds that are easily converted into radicals, such as hydroxyl free radical (HO), hypochlorous acid (HOCl) and hydrogen peroxide (H₂O₂).⁸ Intracellular hepatic lipid accumulation induces oxidative stress during the generation of ROS, which then interact with intracellular proteins, RNA, and DNA, resulting in irreversible damage, hepatocyte apoptosis and the release of inflammatory factors to further promote inflammatory cell

Graphical Abstract



infiltration and activation.⁶ For example, ROS promote M1 macrophage polarization and infiltration; induce the release of proinflammatory cytokines and signaling molecules, including inducible nitric oxide synthase (iNOS), interleukin (IL)-6, IL-1 β , and tumor necrosis factor (TNF)- α ; and promote the progression of MAFLD to MASH.^{7,9,10} Disrupting this cycle between ROS production and inflammation will provide effective treatments for MASH.

MXene nanozymes (MXenzymes) represent a novel class of two-dimensional (2D) metal carbides, comprising ternary metal carbides or nitrides labeled as $M_nA_nX_n$, where M, A, and X denote early d-block transition metals, carbides, nitrides, and carbonitrides, respectively, which are attractive for biosensing and even tissue engineering.¹¹ The novel nanomaterial 2D niobium carbide (Nb_4C_3) MXene nanoenzyme is a transition metal carbide member of the MXene family with an ultrathin layered structure and enzyme-mimicking properties that has attracted much attention for biomedical applications in recent years.^{11–13} For example, Sun et al developed oligo-layer Nb_2C for the treatment of bone tumors, which has the ability to reduce cytokine production and inhibit osteoclastogenesis by promoting the neogenesis and migration of blood vessels.¹⁴ In addition, 2D Nb_2C MXene plate medical implants attenuate excessive inflammatory responses by scavenging excessive ROS in the infected microenvironment.¹⁵ A 2D niobium carbide formulation also combats high blood pressure and promotes diabetic wound healing through highly efficient ROS scavenging and inflammatory factor inhibition.^{16,17} Importantly, studies have shown that niobium carbide has good biocompatibility in cytotoxicity and hemocompatibility experiments both in vitro and in vivo.¹⁸ Therefore, 2D Nb_4C_3 might intrinsically act as a promising antioxidant to treat ROS-related diseases, such as MAFLD.

We speculate that Nb_4C_3 also inhibits macrophage polarization, resists oxidative stress, reduces inflammation, and protects liver function, providing a new direction for the study of Nb_4C_3 in biomedical applications. Here, we present the fabrication, characterization, and application of a single layer of Nb_4C_3 MXene along with in vitro and in vivo studies of its antioxidant and antilipid properties in a MASH mouse model. Nb_4C_3 was rationally designed for biomedical

applications through an etching and exfoliation process; Nb₄C₃ exhibited high concentrations of MXene surface functional groups and surface niobium oxides and niobium carbides (NbC and Nb₂O₅), which contributed to its excellent biocompatibility *in vitro* and *in vivo*.^{19,20} Furthermore, Nb₄C₃ was spontaneously internalized by hepatocytes and macrophages and contributed to reducing liver inflammation through the regulation of M1 macrophage activation and lipid peroxidation. Finally, in a MASH mouse model, tail vein injection of Nb₄C₃ reduced both M1 macrophage infiltration and hepatocyte death. The results of our study may provide new ideas and strategies for the clinical treatment of MASH.

Materials and Methods

Chemicals and Reagents

Aqueous solutions of TPAOH (40%) and LiF were acquired from Adamas-beta Inc. (Shanghai, China). Nb₄AlC₃ was purchased from Feynman Nano Technology Co., Ltd. HCl (36.5–38.0 wt%) and HF were purchased from Sinopharm Chemical Reagent Co., Ltd. (Shanghai, China). Hydrogen peroxide was obtained from Aladdin Ltd. (Shanghai, China). All the chemical reagents were used directly without further purification.

Synthesis of the Nb₄C₃ MXenzyme

Nb₄C₃ MXenzymes were synthesized via a modified liquid-phase exfoliation process.^{11,13,17} Briefly, 2 g of LiF was slowly added to 20 mL of a 9 M HCl aqueous solution for 5 min with agitation to obtain a mixed solution of HCl and LiF. Then, 2 g of Nb₄AlC₃ was slowly added and stirred at 35 °C for 72 h. Subsequently, the Al layers were removed via HF etching, and the suspension was centrifuged at 2000 × g for 10 min and washed several times with DI water until the pH of the supernatant was greater than 6.0. After the last centrifugation cycle, the prepared Nb₄C₃Tx precipitate was dispersed in 200 mL of deionized water and reduced by vacuum degassing for 1 h, followed by ultrasonication for 1 h and centrifugation at 2000 rpm for 1 h. Finally, the suspension was collected and freeze-dried. The samples were further sonicated at 4 °C for 24 h using an SB120-DT ultrasonic cleaner (Ningbo Xinzhi Biotechnology Co., Ltd., China) to obtain ultrathin Nb₄C₃. Nb₄C₃ MXenzymes were dispersed in ultrapure water for different durations, after which the solution was centrifuged for 5 min at 1000 rpm. The supernatant was collected for ICP–OES experiments.

Characterization of the Materials

SEM images were obtained via a Sigma 300 instrument (ZEISS, Germany), and EDS (Bruker Quantax) element maps were obtained at a 15 kV electron acceleration voltage. TEM images were obtained with a Tecnai F20 instrument with the acceleration voltage set to 200 kV. Powder XRD patterns were obtained with a Bruker D8-ADVANCE A25X diffractometer with a Cu K α source in the 2 theta range of 5–95°. XPS was performed on a Scientific K-Alpha photoelectron spectrometer (Thermo Scientific, USA) with Al–K α radiation. Raman spectra were measured with a Horiba JY Lab RAM HR instrument upon excitation with a 532 nm laser at room temperature. EPR was investigated to determine the quantity of ROS via a JEOL JES-FA300 X-band EPR spectrometer (Tokyo, Japan). Briefly, 5 mg of Nb₄C₃ was mixed with 80 mm H₂O₂ and 10 mm FeCl₂. After the samples were allowed to react for 0, 1, 3 or 5 min, 8 mm DMPO was added to the mixture.

Animals and Treatment

WT C57BL/6 mice (aged 6–8 weeks) were purchased from Guangdong Medical Laboratory Animal Center (Guangzhou, China) and housed at the Guangzhou Medical University Animal Experiment Center (Guangzhou, China). All experiments involving animals were conducted according to ethical policies and procedures approved by the Ethics Committee of the Animal Ethics Committee of Guangzhou Medical University (Approval no. 2021031). For the *in vivo* experiments, body weight changes were monitored daily. The concentration of Nb₄C₃ was calculated from Nb as measured by ICP–OES (Agilent Technologies, Palo Alto, CA, USA).

MASH was induced by feeding the mice an MCD (Harlan-Teklad, Indianapolis, IN, USA) for 3 weeks, a time at which steatohepatitis had already been established.²¹ Two groups of C57BL/6 mice were compared (n=6 per group):

mice fed an MCD diet with a tail vein injection of 100 μ L of PBS and mice fed an MCD diet with a tail vein injection of Nb_4C_3 (25 mg/kg, twice a week, total 3 weeks). Liver tissues were collected 3 weeks after the initiation of MCD. Blood was collected immediately prior to sacrifice. Portions of the liver were either frozen immediately in liquid nitrogen or frozen in neutral-buffered formalin.

WT mice were divided into the following two groups to determine the toxicity of Nb_4C_3 in vivo: PBS (tail vein injection of PBS, $n=6$) and Nb_4C_3 (tail vein injection of Nb_4C_3 , $n=6$). The mice were administered 100 μ L of PBS or Nb_4C_3 (25 mg/kg) twice a week for 3 weeks. A routine blood examination was conducted, blood biochemical indices were measured, and major tissues, including the heart, liver, spleen, lung, kidney, and colon, were removed for H&E histological staining.

RNA Isolation and Quantitative Real-Time RT-PCR (qPCR)

Total RNA was extracted with TRIzol reagent (Thermo Fisher Scientific, Waltham, MA, USA), and cDNA was synthesized with PrimeScriptTM RT Master Mix (Takara, Dalian, China). Quantitative real-time PCR was performed with the primers listed in [Supplementary Table 1](#) via SYBR Premix Ex Taq (Vazyme, Nanjing, China) and the Bio-Rad CFX96 System (Bio-Rad Laboratories, CA, USA). The genes were normalized to the expression of the housekeeping gene glyceraldehyde 3-phosphate dehydrogenase (*Gapdh*). Relative mRNA expression was calculated via the comparative $2^{-\Delta\Delta\text{CT}}$ method.

Cell Culture

RAW264.7 cells (a mouse macrophage line) and HepG2 cells (an HCC cell line) were purchased from the Type Culture Collection of the Chinese Academy of Sciences (Shanghai, China) and cultured in medium supplemented with 10% fetal bovine serum. For macrophage generation and differentiation, RAW264.7 cells were pretreated with Nb_4C_3 (200 $\mu\text{g/mL}$) for 12 h and then treated with 100 ng/mL LPS (PeproTech, Rocky Hill, NJ, USA) for 12 h or 24 h to induce their differentiation into M1 macrophages.

HepG2 cells were pretreated with Nb_4C_3 (40 $\mu\text{g/mL}$) for 12 h and then treated with PA (250 μM) (Sigma–Aldrich, St. Louis, MO, USA) for another 12 or 48 h, after which lipid accumulation- and adipogenesis-related protein expression was determined via Oil Red O staining (Sigma–Aldrich), qPCR and Western blotting, respectively. PA was dissolved in DMEM with 2% fatty acid-free bovine serum albumin (BSA, Sigma) after the solvent was evaporated, followed by two rounds of vortexing and 30s of sonication.²²

Cytotoxicity Study

The cytotoxic effects of Nb_4C_3 on HepG2 and RAW264.7 cells were measured via an LDH assay (Beyotime, China) and a Cell Counting Kit-8 (CCK-8, Dojindo Laboratories, Japan). The cells were seeded in 96-well plates at a density of 1×10^3 cells per well. After an overnight incubation, the cells were treated with different concentrations of Nb_4C_3 for 24 hours, and the percentage of viable cells was measured via CCK-8 and LDH kits according to the manufacturer's instructions. The cell viability within each group was reported as a percentage of the viability of untreated control cells.

Uptake of Nb_4C_3

Nb_4C_3 was incubated with 3,3'-diiodo-4,4'-dimethoxydiphenylmethane perchlorate (DIO) (Beyotime Institute of Biotechnology, Shanghai, China) for 30 min and then washed to remove the excess dye. DIO- Nb_4C_3 was incubated with RAW264.7 cells and HepG2 cells for 12 h and then imaged with a Leica DMI8 microscope (Leica, Wetzlar, Germany).

Live/Dead Cell Double Staining

Live/dead cell double staining was performed via a Calcein AM/PI double staining kit (Beyotime Institute of Biotechnology) according to the manufacturer's instructions. Briefly, adherent HepG2 cells were pretreated with Nb_4C_3 for 12 h and then treated with H_2O_2 (1 mM) for 10 h or PA (250 μM) for 24 h, after which the cells were washed twice with cold PBS and incubated with buffer containing calcein AM and propidium iodide (PI) at room

temperature for 15–30 min. Then, the fluorometric signals of live cells (green fluorescence) and dead cells (red fluorescence) were immediately visualized with a Leica DMI8 microscope (Leica, Wetzlar, Germany).

ROS Assay

We chose a ROS assay kit (Beyotime Institute of Biotechnology) to measure the intracellular ROS levels according to the manufacturer's protocol. Briefly, RAW264.7 macrophages were pretreated with Nb₄C₃ (200 µg/mL) for 12 h and then treated with 100 ng/mL LPS for 24 h; HepG2 cells were pretreated with Nb₄C₃ (200 µg/mL) for 12 h and then treated with PA (250 µM) for another 48 h. Then, the cells were incubated with the DCFH-DA (20 µM) probe in an incubator for 20 min. The cells were observed with a Leica DMI8 microscope.

Flow Cytometry Analysis

Flow cytometry was used to detect macrophage polarization. RAW264.7 cells were pretreated with Nb₄C₃ (40 µg/mL) for 12 h and then treated with 100 ng/mL LPS for 24 h. M1 macrophages were labeled with antibodies against F4/80-FITC (eBioscience, San Diego, CA, USA), MHC II-PE (eBioscience) and CD206-APC (eBioscience).

HepG2 cells were analyzed via an Annexin V-FITC apoptosis detection kit (Beyotime, China) to determine the percentage of apoptotic cells. After PA treatment for 48 h, the cells were harvested and resuspended in binding buffer containing Annexin V-FITC and PI. Flow cytometry was performed on a FACSVerse cytometer, and the data were subsequently analyzed via FlowJo 10.0 (Tree Star, Ashland, OR, USA).

Western Blot Analysis

For Western blot analyses, total protein samples were extracted from tissues with RIPA lysis buffer supplemented with protease inhibitor cocktail tablets and phosphatase inhibitor tablets (Roche, Basel, Switzerland). Anti-SREBP1, anti-PPAR γ , anti-p44/42 MAPK (pErk1/2), anti-p44/42 MAPK (Erk1/2), anti-p38 MAPK, anti-p38 MAPK, anti-p-NF- κ B p65 and anti-NF- κ B p65 antibodies were purchased from Cell Signaling Technology (CST, Beverly, MA, USA), and the anti-GAPDH primary antibody was purchased from Zhonshanjinqiao (Wuhan, China). A Gene5 image acquisition system (Syngene, Frederick, MD, USA) was used for signal detection.

ELISAs

RAW264.7 cells were pretreated with Nb₄C₃ for 12 h and then treated with 100 ng/mL LPS for 24 h. After the cell supernatants were harvested, the concentrations of IL-6 and TNF α were determined via ELISA kits (4A Biotech, Beijing, China). The samples were tested in triplicate.

Liver tissues were lysed in RIPA buffer, and the total protein concentration was determined with a BCA protein assay (Beyotime). Five hundred micrograms of total protein lysate was subjected to ELISA to detect IL-1 β and IL12p40 levels. Protein levels were normalized to the total protein concentration.

MDA, GSH and SOD Assays

MDA, GSH and SOD assays were conducted via the Lipid Peroxidation MDA Assay Kit (Beyotime) according to the manufacturer's instructions. The samples and standards were prepared, and the OD value was measured at 532 nm. The MDA and GSH concentrations (nmol/mL) are reported as µmol/mg protein. SOD activity is reported as U/mg protein.

Mouse Blood Biochemical Analyses

Commercial kits were used to measure the serum ALT, AST, BUN, Cr, CK, and LDH levels (Jiancheng Institute of Biotechnology, Nanjing, China) according to the manufacturer's instructions.

Oil Red O Staining

Liver tissues were embedded in optimal cutting temperature (OCT) compound and then frozen at −20 °C. Frozen sections (10 µm) were stained with Oil Red O (O0625, Sigma) and counterstained with Mayer's hematoxylin to visualize intracellular lipid droplets. All digital images were obtained with a Leica DM6 microscope (Leica).

Hepatic Lipid Analyses

A commercial kit was used to measure TAG and TC levels (Jiancheng Institute of Biotechnology) in the liver and TAG levels in cells.

Histological Scoring

Liver sections were cut and fixed with 4% paraformaldehyde, stained with H&E, and examined under a Leica DM6 microscope for histological evaluation. The lesions in the liver sections were evaluated histologically according to the NASH CRN scoring system, as previously reported.^{23,24}

Immunohistochemistry

Deparaffinized liver sections were immunostained for PPAR γ (Cell Signaling Technology), SREBP1 (Cell Signaling Technology), F4/80 (Abcam, Cambridge, MA, USA), iNOS (Abcam) and cleaved caspase-3 (Abcam) antibodies. The immunostained sections were examined with a Leica DM6 microscope. The IHC Profiler in ImageJ was used to assess the degree of staining.

Statistical Analysis

The results are reported as the means \pm standard deviations (SDs). SPSS 21.0 software (SPSS Inc., Chicago, USA) was used for the analysis. Differences between groups were compared via Student's *t* test or one-way ANOVA with post hoc tests when applicable or with a nonparametric test. **p*<0.05, ***p*<0.01, and ****p*<0.001 were considered statistically significant.

Results and Discussion

Synthesis and Characterization of Nb₄C₃

We prepared Nb₄C₃ through hydrofluoric acid (HF) etching of Nb₄AlC₃ powder followed by intercalation with tetrapropylammonium hydroxide (TPAOH) and repeated ultrasonication and centrifugation steps to obtain ultrathin layered Nb₄C₃.^{18,25} Crucially, this two-step exfoliation process can be scaled to prepare large quantities of high-quality Nb₄C₃, which can be well dispersed in water for long-term storage ([Supplementary Figure 1](#)). Next, scanning electron microscopy (SEM) revealed that Nb₄C₃ exhibited the typical accordion structures of MXenes ([Figure 1A](#)), and energy-dispersive spectroscopy (EDS) revealed that Nb₄C₃ contained Nb, C, and O ([Figure 1B](#)). These results clearly indicate that significant amounts of Al were removed from the MAX phase structure in Nb₄AlC₃. The TEM image further showed revealed that Nb₄C₃ had stacked basal planes in the MXene layers ([Figure 1C](#)). Furthermore, high-resolution TEM (HRTEM) and selected area diffraction (SAED) analyses indicated that the exfoliated Nb₄C₃ MXene flakes possessed a symmetric crystalline structure consisting of layers with a d-spacing of ≈ 0.2455 nm, which can be assigned to the (111) plane ([Figure 1D](#) and [E](#)). Taken together, these findings provide robust evidence that crystalline Nb₄C₃ was successfully fabricated via a two-step exfoliation strategy.

We further characterized the structural characteristics of Nb₄C₃ via X-ray diffraction (XRD), which uses Cu-K α radiation to assess the phase purity and structural properties. The main characteristic peak of MXene clearly emerged at $\approx 15^\circ$ 2 θ in the Nb₄C₃ sample, and characteristic Nb₄C₃ and Nb₂O₅ peaks were observed in Nb₄C₃, indicating that Nb₄C₃ had an oxidized surface ([Figure 2A](#)). Additionally, a minor amorphous curve between 10° and 90° 2 θ indicated the presence of carbon formed during the ultrasonication process ([Figure 2A](#)). The Raman spectrum revealed characteristic peaks of Nb₄C₃ at 1323 and 1586 cm⁻¹ (namely, Nb-C) ([Figure 2B](#)), and X-ray photoelectron spectroscopy (XPS) revealed apparent decreases in the intensities of the Nb 3d₅, C 1s and O 1s spectra. These results further indicated the generation of high-quality Nb₄C₃ during synthesis ([Figure 2C](#)). Additionally, the Nb 3d₅ XPS spectrum ([Figure 2D](#)) showed two dominant signals belonging to Nb 3d (203 eV) and Nb 3d_{5/2} (207.5 eV), representing Nb₄C₃ and Nb₂O₅, respectively. The formation of transition metal oxides during hydrothermal processes has been reported.²⁶ Remarkably, the Nb-O peaks of Nb 3d_{5/2} and 3d_{3/2} located at ≈ 207.5 and 210 eV were enhanced ([Figure 2D](#)). Additionally, the high-resolution C 1s spectrum of Nb₄C₃ included a combination of C-C/ C-H, C-O and C=O peaks fitted at binding energies between 285 and 287.5 eV ([Figure 2E](#)). The O 1s spectrum contained

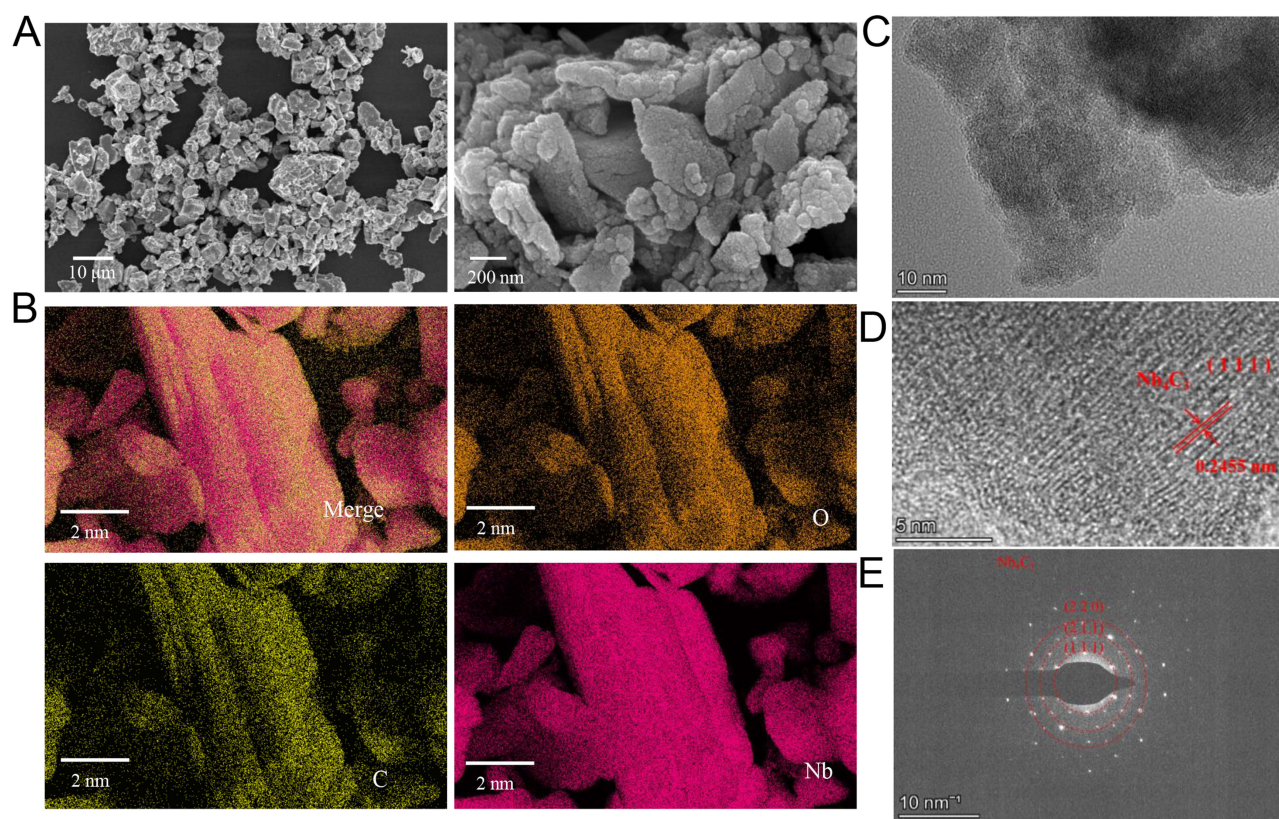


Figure 1 The morphology of Nb_4C_3 . (A) SEM image of Nb_4C_3 . (B) Corresponding energy-dispersive spectroscopy element maps of Nb, C and O. (C and D) High-resolution TEM (HRTEM) images of the Nb_4C_3 nanosheets revealed well-defined and exfoliated crystals with a lattice d-spacing of ≈ 0.2455 nm. (E) The corresponding SAED pattern of Nb_4C_3 .

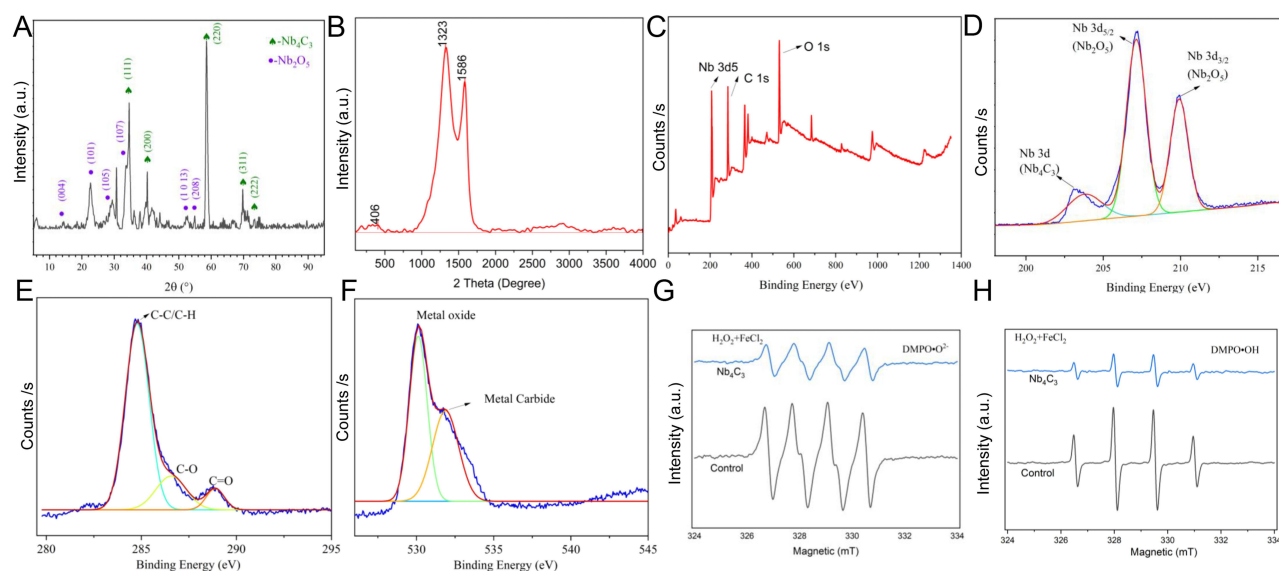


Figure 2 Characterization of the structure, functional groups, chemical composition and superior ROS scavenging efficacy of Nb_4C_3 . (A) XRD patterns of Nb_4C_3 . (B) Raman spectra of Nb_4C_3 . (C) XPS survey patterns of Nb_4C_3 . (D-F) High-resolution XPS spectra of Nb 3d (D), C 1s (E) and O 1s (F). (G and H) EPR spectra of Nb_4C_3 DMPO-OH (G) and DMPO- O_2^- adducts (H) at different times.

peaks between 530 and 535 eV, indicating a high level of oxygen-containing functional groups on the surfaces of the Nb_4C_3 molecules (Figure 2F). Consistent with our XRD characterization results, the XPS analysis results indicated that the as-synthesized Nb_4C_3 was suitable for targeted application.

We used the electron paramagnetic resonance (EPR) approach to evaluate the ROS scavenging efficiency. Before 5,5-dimethyl-1-pyrroline N-oxide (DMPO) was added to trap $\cdot\text{OH}$ and $\cdot\text{O}^{2-}$, quantitative amounts of FeSO_4 and H_2O_2 were used to generate ROS via the Fenton reaction.⁶ Five minutes after adding Nb_4C_3 to the solution, the peak intensities of $\text{DMPO}\cdot\text{OH}$ and $\text{DMPO}\cdot\text{O}^{2-}$, which result from the interaction of unabsorbed ROS with DMPO, were evaluated to test the ability of Nb_4C_3 to scavenge ROS. As depicted in [Figure 2G](#) and [H](#), Nb_4C_3 showed potent ROS scavenging activity, leading to a decrease in the peak intensities of $\text{DMPO}\cdot\text{OH}$ and $\text{DMPO}\cdot\text{O}^{2-}$ ([Figure 2G](#) and [H](#)). We employed XPS to observe the alterations in Nb_4C_3 stability and the changes in the oxidation products following H_2O_2 treatment. The XPS survey patterns, Nb 3d_{5/2} spectra and C 1s spectra of the oxidized Nb_4C_3 were essentially identical to those of the original unoxidized Nb_4C_3 ([Supplementary Figure 2A–C](#)). Additionally, we used EPR to examine the ROS scavenging ability of Nb_4C_3 , both with and without H_2O_2 treatment. Following incubation at the same concentration, the absorption peaks for $\text{DMPO}\cdot\text{OH}$ and $\text{DMPO}\cdot\text{O}^{2-}$ remained unchanged ([Supplementary Figure 2D](#) and [E](#)). These results indicated the excellent ROS trapping efficiency and stability of Nb_4C_3 .

Biocompatibility of Nb_4C_3

Macrophages and hepatocytes, which are the primary types of immune and parenchymal liver cells, play significant roles in lipid peroxidation, oxidative stress, inflammation, and fibrosis associated with steatohepatitis.²⁷ We stimulated RAW264.7 and HepG2 cells with various concentrations (50 $\mu\text{g/mL}$, 100 $\mu\text{g/mL}$, 200 $\mu\text{g/mL}$, or 400 $\mu\text{g/mL}$) of Nb_4C_3 for 24 h and then assessed the relative cell viability via a Cell Counting Kit-8 (CCK-8) assay. As the Nb_4C_3 concentration increased, the relative cell viability did not decrease ([Figure 3A](#)). The amount of lactate dehydrogenase (LDH) released from the cells was assessed and did not increase significantly after treatment with increasing Nb_4C_3 concentrations ([Figure 3B](#)). These results indicate that Nb_4C_3 had no significant effect on the relative viability of RAW264.7 and HepG2 cells.

MXenes can trigger the release of proinflammatory cytokines from tissue macrophages by increasing ROS levels, potentially disrupting the anti-inflammatory and immunomodulatory characteristics of the liver.²⁸ Therefore, we stimulated RAW264.7 cells with 100 ng/mL lipopolysaccharide (LPS) as a positive control and stimulated cells in the experimental group with different concentrations of Nb_4C_3 alone. The expression of the proinflammatory cytokines *Tnfa*, *Il6*, *Il12p40* and *inos* was significantly increased in the LPS group, whereas the expression of these proinflammatory cytokines did not increase in the group treated with Nb_4C_3 alone ([Figure 3C](#)). Moreover, different variants of MXenes, such as titanium carbide MXene nanosheets ($\text{Ti}_3\text{C}_2\text{Tx}$ MXenes), can induce cell death by increasing cellular oxidative stress.¹³ Therefore, we performed live/dead cell double-staining assays using HepG2 cells and a calcein/propidium iodide (PI) cell activity kit. The HepG2 cells were cultured with or without different doses of Nb_4C_3 for 24 h, and as the concentration of Nb_4C_3 increased, no increase in red fluorescence (dead cells) was observed ([Figure 3D](#)), suggesting that Nb_4C_3 does not induce HepG2 cell death, likely because its concentration was below the toxicity threshold. We subsequently examined whether Nb_4C_3 was internalized by HepG2 and RAW264.7 cells. Nb_4C_3 was labeled with a 3,3'-dioctadecyloxacarbocyanine perchlorate (DIO) green fluorescent probe, after which the cells were incubated with DIO-labeled Nb_4C_3 for 12 h. The cells were then fixed and stained with 4',6-diamidino-2-phenylindole (DAPI) to visualize the nuclei (light blue). The green fluorescence of the Nb_4C_3 particles and the blue fluorescence of the cell nuclei revealed that Nb_4C_3 was phagocytosed into the cytoplasm of the RAW264.7 and HepG2 cells ([Figure 3E](#)).

Next, we studied the distribution of Nb_4C_3 in the primary organs of the mice. The mice were injected with Nb_4C_3 via the tail vein for 3 weeks, and the level of elemental Nb in major organs was measured via inductively coupled plasma atomic emission spectrometry (ICP–OES). Nb_4C_3 was not detected in any major organ other than the liver (<1.25 $\mu\text{g/g}$ tissue) ([Figure 3F](#)). The possible harmful effects of Nb_4C_3 were further assessed through blood analysis and histological studies. The serum alanine aminotransferase (ALT), aspartate aminotransferase (AST), urea nitrogen (BUN), creatinine (Cr), creatine kinase (CK) and LDH levels indicated that Nb_4C_3 had no significant effects on liver, heart, or kidney function ([Figure 3G](#)). Hematoxylin and eosin (H&E) staining also revealed no apparent tissue damage or adverse effects in the Nb_4C_3 group ([Figure 3H](#)). Both groups of mice exhibited no notable adverse reactions, suggesting that Nb_4C_3 could be utilized for future in vivo biomedical studies.

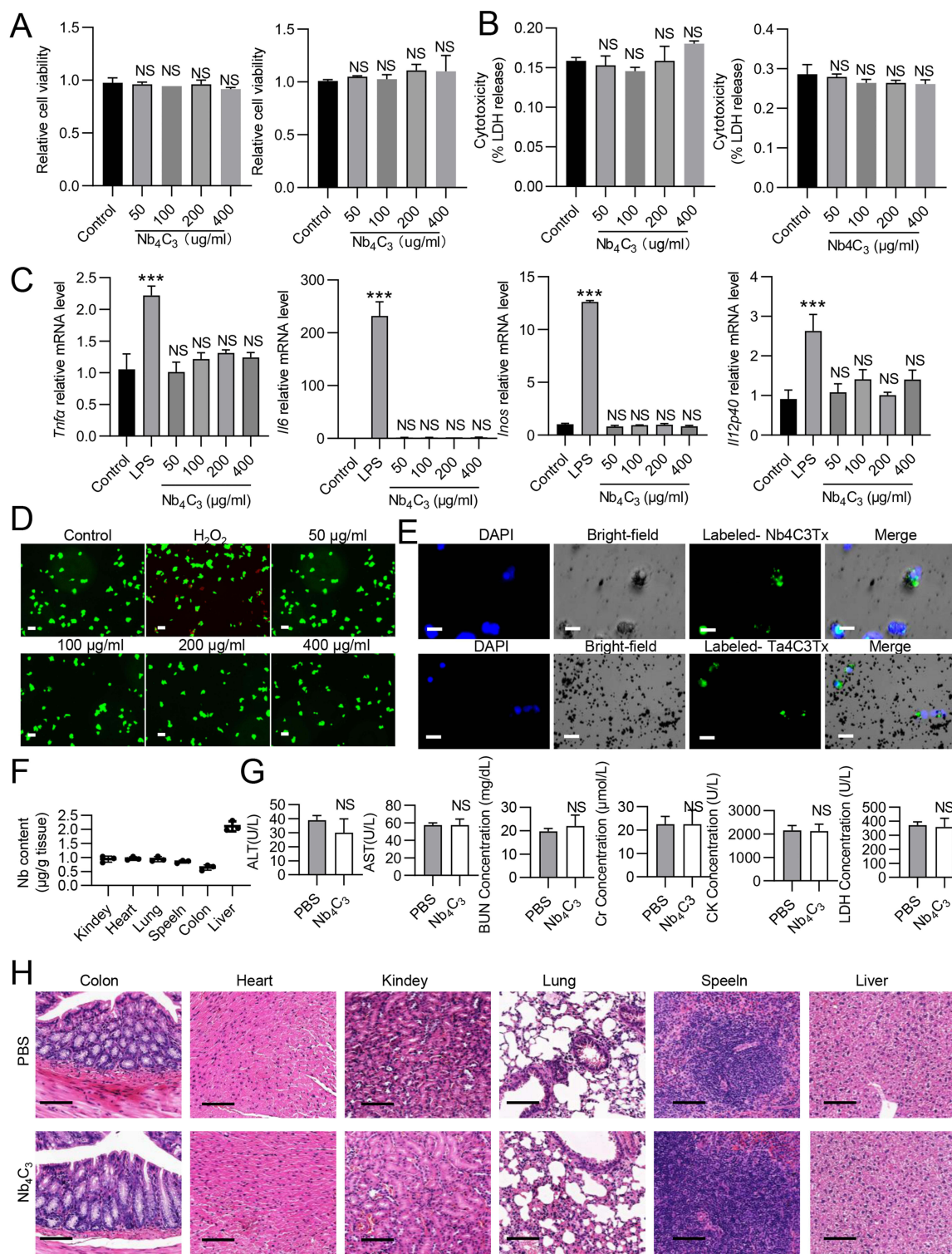


Figure 3 Evaluation of the cellular compatibility and biosafety of Nb₄C₃. **(A)** The viability of RAW264.7 and HepG2 cells after 24 h of coculture with different concentrations of Nb₄C₃ was measured via CCK-8 assays. **(B)** The death of RAW264.7 and HepG2 cells after 24 h of coculture with different concentrations of Nb₄C₃ was measured via an LDH Cytotoxicity Assay Kit. **(C)** RAW264.7 cells were cocultured with different concentrations of Nb₄C₃ for 12 h. The levels of proinflammatory factors (*Tnfα*, *Il6*, *Il12p40* and *inos*) were measured. **(D)** Image of live/dead fluorescence staining of HepG2 cells (live cells: green; dead cells: red; scale bar = 75 µm). H₂O₂ was used as a positive control. **(E)** Uptake of Nb₄C₃ by RAW264.7 and HepG2 cells. RAW264.7 and HepG2 cells were incubated with DIO-labeled Nb₄C₃ (green) and analyzed by immunofluorescence staining. Scale bars = 25 µm. **(F–H)** C57BL/6 mice were subjected to a tail vein injection of 100 µL of PBS or Nb₄C₃ (25 mg/kg). **(F)** Nb levels in the different tissues determined by ICP-OES. **(G)** Blood biochemical (BUN, Cr, CK, and LDH) tests were performed. **(H)** H&E staining of the heart, liver, spleen, lung, kidney, and colon. The data are presented as the means ± SDs. ***P < 0.001.

Abbreviation: NS, not significant.

In vitro Macrophage Polarization and Anti-Inflammatory Properties of Nb₄C₃

Kupffer cells are the most abundant immune cells and play a critical role in liver homeostasis and disease; these cells reside in liver sinusoids and are first-line responders to any pathogen.²⁹ Kupffer cells can adopt an M1 (proinflammatory) phenotype or an M2 (anti-inflammatory) phenotype, and the number of M1 macrophages significantly increases as MASH progresses.^{10,28,30,31} Owing to their surface activity, MXenes have drawn considerable attention because they can mitigate proinflammatory responses by removing excessive ROS in infectious microenvironments, which supports tissue remodeling.^{14,30} The direct interactions of Nb₄C₃ with RAW264.7 cells were investigated to assess its effects on M1 macrophages. We detected considerably higher levels of *Inos* and *Il12p40* (M1 biomarkers) in the positive control group after lipopolysaccharide (LPS) treatment than in the control group (Figure 4A). Compared with those in the LPS group, the groups treated with different concentrations of Nb₄C₃ presented significantly lower expression levels of *Inos* and *Il12p40* (Figure 4A). Nb₄C₃ treatment significantly reduced the expression of *Tnfa* and *Il6*, with the most potent effect of Nb₄C₃ observed at concentrations of 200 and 400 µg/mL (Figure 4A). Therefore, a dose of 200 µg/mL was chosen for subsequent experiments. Nb₄C₃ treatment significantly decreased the percentage of MHC II (M1 marker)-positive cells and increased the percentage of CD206 (M2 marker)-positive cells (Figure 4B), confirming that Nb₄C₃ induced M1 to M2 macrophage polarization. Treatment of RAW264.7 macrophages with Nb₄C₃ significantly inhibited the release of IL-6 and TNF-α (Figure 4C). These results indicate that Nb₄C₃ treatment can inhibit M1 macrophage polarization.

Since ROS play crucial roles in M1 macrophage differentiation and activation,³² the 1,2,7-dichlorofluorescein diacetate (DCFH-DA) probe, which reacts with intracellular ROS and generates green fluorescent DCF, was used to analyze the ability of Nb₄C₃ to scavenge ROS. We observed a stronger green fluorescent signal in the LPS-treated RAW264.7 cells than in the untreated or Nb₄C₃-treated cells (Figure 4D). After pretreatment with Nb₄C₃, the DCF fluorescence signal markedly decreased in the LPS-treated cells, suggesting that most of the intracellular ROS were eliminated by Nb₄C₃. Excessive ROS can induce oxidative stress and activate proinflammatory signaling pathways, including the nuclear factor-κB (NF-κB) and mitogen-activated protein kinase (MAPK) pathways, thereby aggravating inflammation.^{6,7} Therefore, we analyzed the effects of Nb₄C₃ on proinflammatory signaling pathways. Nb₄C₃ not only suppressed the NF-κB pathway but also inhibited the activation of the ERK MAPK and p38 MAPK signaling pathways, which are master inflammation-related transcription factors and inflammatory signaling pathways (Figure 4E). The results of these experiments indicate that Nb₄C₃ reduces ROS production and ROS-induced inflammation in RAW264.7 macrophages.

Nb₄C₃ Alleviates ROS and Lipotoxicity in Fatty Hepatocytes

Lipid droplet formation in hepatocytes induces lipotoxicity and oxidative stress through the accumulation of ROS, leading to hepatocyte apoptosis and the progression of inflammation.^{6,28} In vitro, a hepatocyte lipid droplet model was constructed by incubating HepG2 cells (a human hepatic carcinoma cell line) with 250 µM palmitic acid (PA). Intracellular lipid droplet formation was assessed in Nb₄C₃-treated HepG2 cells in response to PA to confirm the ability of Nb₄C₃ to inhibit lipid droplet accumulation. The number and size of the lipid droplets clearly increased in the PA group, and lipid droplet formation in HepG2 cells decreased after Nb₄C₃ treatment; these results were supported by the results of the quantitative analysis (Figure 5A). A reduction in TAG content was also observed after Nb₄C₃ treatment (Figure 5B). The expression levels of adipogenesis-related genes during lipid droplet formation were assessed by qPCR and Western blotting to further confirm the lipid-lowering effect of Nb₄C₃. The results revealed that the expression levels of fatty acid regulatory genes (*sterol regulatory element-binding protein 1* (*Srebp1*)) and master transcription factors involved in adipogenesis (*peroxisome proliferator-activated receptor γ* (*Pparγ*)) were significantly increased after PA treatment and decreased after Nb₄C₃ treatment (Figure 5C). SREBP1 and PPARγ protein expression was also lower in the Nb₄C₃ treatment group than in the PA treatment group (Figure 5D).

Oxidative stress induced by excessive ROS generation induces lipid peroxidation,³³ thus, the ability of Nb₄C₃ to scavenge intracellular ROS was investigated in vitro. PA treatment clearly induced an intracellular oxidative response, as evidenced by an increase in the malondialdehyde (MDA) content and decreases in the glutathione (GSH) and superoxide dismutase (SOD) contents, effects that were reversed by Nb₄C₃ treatment (Figure 5E). In addition, the DCFH-DA probe was used to assess whether Nb₄C₃ could scavenge intracellular ROS. As shown in Figure 5F, compared with the other

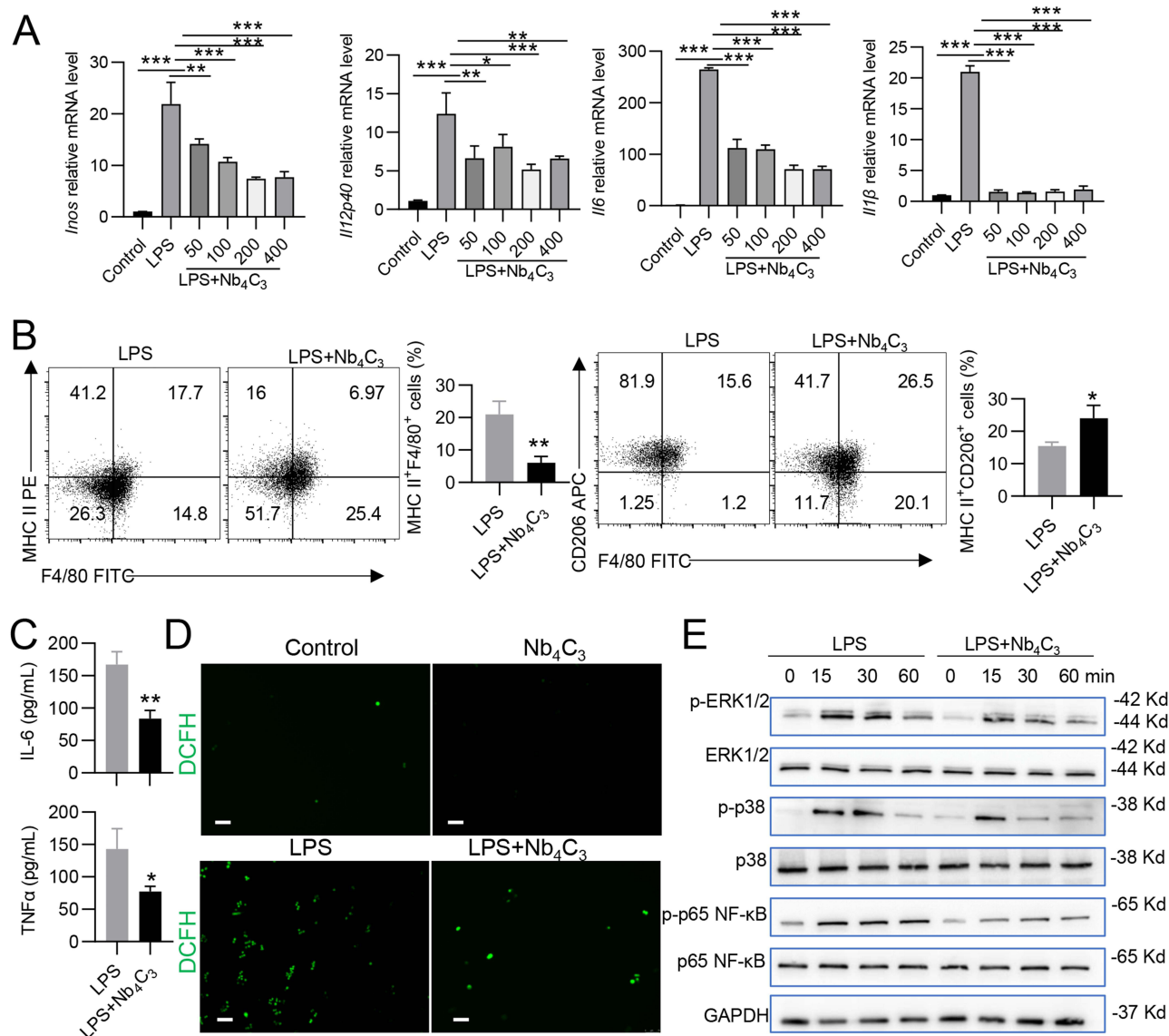


Figure 4 Antioxidant, anti-inflammatory, and macrophage polarization properties of Nb₄C₃. **(A)** RAW264.7 cells were cocultured with different concentrations of Nb₄C₃ for 12 h in the presence of LPS. The levels of proinflammatory factors (*Tnfa*, *Il6*, *Il12p40* and *inos*) were measured. RAW264.7 cells were cocultured with different concentrations of Nb₄C₃ for 24 h in the presence of LPS, and the numbers of F4/80⁺MHC II⁺ cells and F4/80⁺CD206⁺ cells were analyzed by flow cytometry **(B)**. The concentrations of TNF- α and IL6 in the cell supernatants were detected **(C)**, and images of the ROS levels were captured. ROS (green) were labeled with DCFH (scale bar = 75 μ m) **(D)**. **(E)** Changes in the levels of p-ERK1/2, p-P38 and p-p65 NF- κ B after treatment with Nb₄C₃. The data are presented as the means \pm SDs. *P < 0.05, **P < 0.01, and ***P < 0.001.

groups, the PA group presented the strongest ROS fluorescence signal, and Nb₄C₃ intervention markedly reduced the PA-induced increase in the ROS content, suggesting that most of the intracellular ROS were scavenged by Nb₄C₃. Moreover, we evaluated the protective effect of Nb₄C₃ by performing live/dead cell staining and flow cytometry analysis. PA treatment markedly increased the number of dead cells (red fluorescence), but a marked decrease in the number of dead cells was observed in the Nb₄C₃ treatment group (Figure 5G). In addition, PA treatment markedly increased HepG2 cell apoptosis, but Nb₄C₃ treatment reduced HepG2 cell apoptosis (Figure 5H). During lipid peroxidation, hepatocyte injury and apoptosis induce proinflammatory cytokine release.⁶ As shown in [Supplementary Figure 3](#), Nb₄C₃ treatment reduced the PA-induced increase in the expression of the proinflammatory genes *Tnfa*, *Il6* and *Il1β*. Thus, cell death caused by oxidative stress can be prevented by Nb₄C₃ in vitro through its ability to scavenge ROS.

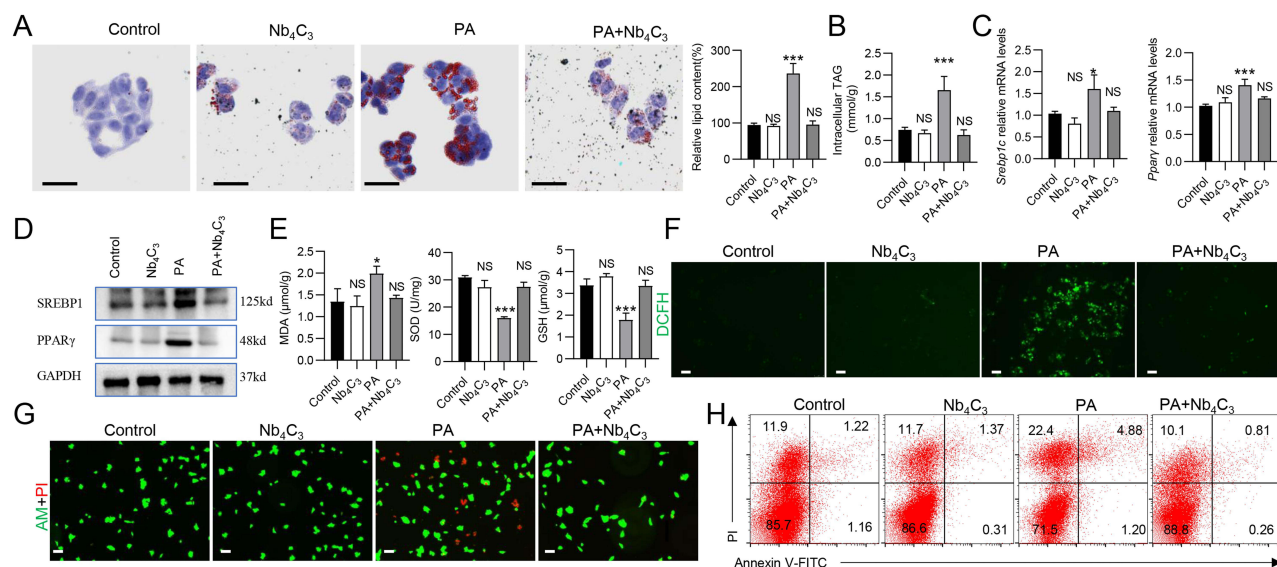


Figure 5 Antioxidant, anti-inflammatory, and antisteatotic activity of Nb₄C₃ in HepG2 cells. The cells were pretreated with Nb₄C₃ for 12 h and then treated with PA (250 μM) for 12 or 48 h. **(A)** Oil red O staining was performed to determine lipid accumulation. Scale bar, 25 μm. **(B)** Intracellular TAG levels were measured via a TAG test kit. **(C)** The relative expression of *Pparγ* and *Srebp1* was determined via RT-qPCR. **(D)** Western blotting was performed to determine the PPARγ and SREBP1 protein levels, and the results were normalized to those of GAPDH. **(E)** Intracellular SOD activity and GSH and MDA levels were assayed according to the manufacturer's instructions. **(F)** Representative images of HepG2 cells stained with DCFH-DA after various treatments, as indicated. **(G)** Live (green)/dead (red) cell double staining of HepG2 cells incubated with PA in the absence or presence of Nb₄C₃. **(H)** PA-induced apoptosis of HepG2 cells treated with or without Nb₄C₃. *P < 0.05; and ***P < 0.001. **Abbreviation:** NS, not significant.

Antioxidant and Anti-Inflammatory Effects of Nb₄C₃ in vivo

MCD-induced acute MASH involves crosstalk between oxidative stress and inflammatory responses, and antioxidants can suppress proinflammatory responses and cell injury in individuals with MASH.³⁴ Owing to the antioxidant and anti-inflammatory activities of Nb₄C₃, an MCD-induced MASH mouse model was established to evaluate the role of Nb₄C₃ in MASH. After 3 weeks of MCD diet feeding, the body weights of the mice decreased markedly, indicating successful establishment of the MASH model (Figure 6A), and none of the mice died. Nb₄C₃ treatment did not alleviate weight loss in MASH mice (Figure 6A) but significantly increased the liver-to-body weight ratio (Figure 6B). Furthermore, pathological hematoxylin and eosin (H&E) and Oil Red O staining revealed that the MCD+PBS group presented obvious lipid droplets and inflammatory features, including hepatocyte vacuolization and inflammatory cell infiltration (Figure 6C). Compared with those in tissues from mice in the MCD+PBS group, lipid droplet accumulation and inflammatory cell infiltration were obviously lower in tissues from mice in the MCD+Nb₄C₃ group, indicating that Nb₄C₃ inhibited MASH progression (Figure 6C). In addition, the total cholesterol (TC) and TAG levels in the liver were significantly lower in the Nb₄C₃ treatment group than in the control group (Figure 6D). Biochemical studies revealed that the plasma alanine aminotransferase (ALT) and aspartate aminotransferase (AST) levels were significantly decreased after Nb₄C₃ treatment (Figure 6E).

We used ICP-OES to determine the Nb concentration in the liver, and the Nb concentration was 4-fold greater in the MCD+Nb₄C₃ group than in the control group (Figure 6F). Next, the level of lipid peroxidation was detected in the liver after treatment with Nb₄C₃ by measuring the MDA, SOD, and GSH levels. The MDA level significantly decreased, and the GSH and SOD levels significantly increased after Nb₄C₃ treatment (Figure 6G). A quantitative polymerase chain reaction (qPCR)-based analysis of the expression of proinflammatory factors and adipogenic-related genes was performed to obtain insights into the mechanisms by which Nb₄C₃ exerts its antioxidant and anti-inflammatory effects. Nb₄C₃ significantly reduced the levels of the proinflammatory factors *Tnfa*, *Il6*, *Il1β* and *Inos* (Figure 6H). Significant decreases in the expression of adipogenic markers, such as *Srebp1* and *Pparγ*, and key enzymes that regulate cellular fatty acids, such as acetyl-CoA carboxylase (*Acc*) and fatty acid synthase (*Fasn*), were also observed (Figure 6H). Furthermore, PPAR and SREBP1 expression was assessed via immunohistochemical staining (Figure 6I). Compared with MASH model mice treated with PBS, MASH model mice treated with Nb₄C₃ presented significantly lower expression of cleaved caspase 3 in the liver, which was consistent with the antiapoptotic effect on HepG2 cells in vitro (Figure 6J). Immunohistochemistry for F4/80 and iNOS,

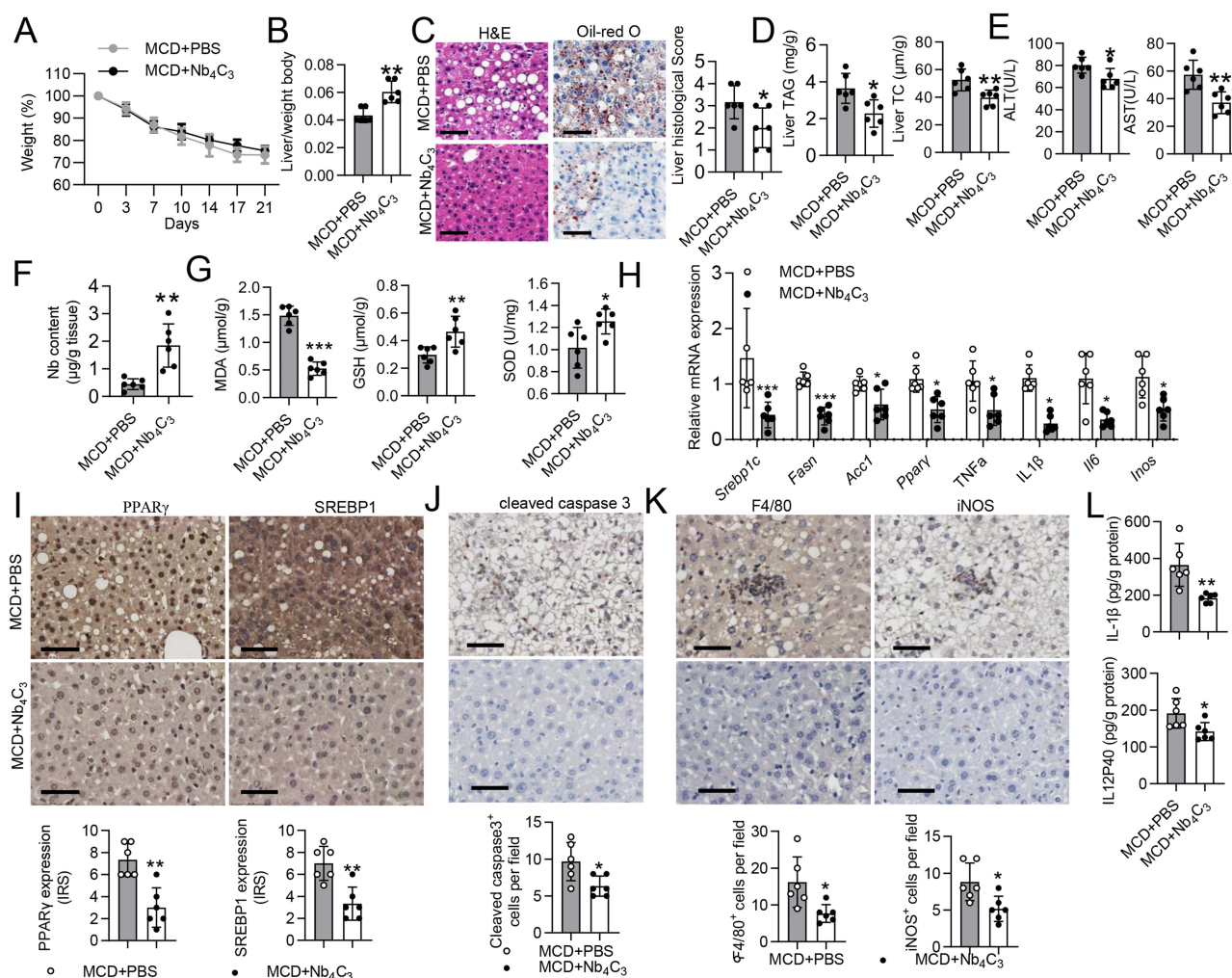


Figure 6 Nb₄C₃ reduced hepatic steatosis and inflammation in the MASH model. C57BL/6 mice were fed an MCD for 3 weeks and received a tail vein injection of 100 μL of PBS or Nb₄C₃. (A and B) Body weights and liver/weight ratios of the mice. (C) Representative H&E-stained and Oil Red O-stained liver sections from the different groups. Scale bar, 50 μm. Histological scores of the liver tissue from the two groups described above. (D) TAG and TC levels in the liver. (E) Serum levels of ALT and AST. (F) Nb levels in the liver tissue were determined via ICP-OES. (G) Liver SOD activity and GSH and MDA levels were assayed according to the manufacturer's instructions. (H) The levels of proinflammatory factors (*Tnfa*, *Il6*, *Inos* and *Il1β*) and fatty acid regulatory factors (*Srebp1*, *Fasn*, *Acc* and *Pparγ*) were measured via qPCR. Gene expression was normalized to *Gapdh*. (I–K) Representative images of PPARγ, SREBP1, cleaved caspase3, F4/80 and iNOS immunohistochemical staining of liver tissue sections are shown. Scale bar = 50 μm. (L) The concentrations of IL12p40 and IL-1β in liver tissue were measured via ELISA. The data are presented as the means ± SDs. *P < 0.05, **P < 0.01 and ***P < 0.001.

which are markers of macrophages and M1 macrophages, respectively, was performed to quantify macrophage infiltration.³⁵ F4/80 and iNOS levels were significantly lower in liver tissues from mice treated with Nb₄C₃ than in those from mice treated with PBS (Figure 6K). Furthermore, Nb₄C₃ treatment decreased the levels of IL-1β and IL12p40, which are proinflammatory cytokines (Figure 6L). These results suggest that Nb₄C₃ reverses macrophage polarization from the M1 phenotype to the M2 phenotype and regulates the secretion of various cytokines within the liver to relieve MASH symptoms.

Conclusions

In this work, we described the antioxidant and antilipid activities of Nb₄C₃ in a MASH mouse model. On the one hand, Nb₄C₃ can inhibit hepatocyte lipid accumulation and disrupt lipid metabolism, subsequently reducing lipid peroxidation-associated hepatocyte death. On the other hand, Nb₄C₃ significantly inhibits inflammation by decreasing ROS levels and the secretion of proinflammatory cytokines to inhibit the polarization of M1-phenotype macrophages, thereby efficiently alleviating MAFLD symptoms. In conclusion, Nb₄C₃, which has multiple bioactivities, may have promising applications in the treatment of MASH.

Abbreviations

MASH, metabolic dysfunction-associated steatohepatitis; 2D, two-dimensional; ROS, reactive oxygen species; Nb₄C₃, niobium carbide; MXenzymes, MXene nanoenzymes; MCD, methionine–choline-deficient diet; MAFLD, metabolic dysfunction-associated fatty liver disease; RO₂, peroxy radical; RO, alkoxyl radical; O₂^{•−}, superoxide radical; HO₂, hydroperoxyl radical; HOCl, hypochlorous acid; H₂O₂, hydrogen peroxide; Inos, inducible nitric oxide synthase; ILs, interleukins; TNF, tumor necrosis factor; TPAOH, tetrapropylammonium hydroxide; LiF, lithium fluoride; HF, hydrofluoric acid; SEM, scanning electron microscopy; EDS, energy-dispersive spectroscopy; TEM, transmission electron microscopy; XRD, X-ray diffraction; XPS, X-ray photoelectron spectroscopy; EPR, electron paramagnetic resonance; ICP–OES, inductively coupled plasma–atomic emission spectrometry; PBS, phosphate-buffered saline; H&E, hematoxylin and eosin; qPCR, quantitative real-time RT–PCR; GAPDH, glyceraldehyde 3-phosphate dehydrogenase; LPS, lipopolysaccharide; PA, palmitic acid; BSA, bovine serum albumin; LDH, lactate dehydrogenase; CCK-8, Cell Counting Kit-8; DIO, 3,3′-diocetadecyloxacarbocyanine perchlorate; DCFH-DA, 2,2′-dichlorofluorescein diacetate; SREBP1, sterol regulatory element-binding protein 1; PPARγ, peroxisome proliferator-activated receptor γ; MDA, malondialdehyde; GSH, glutathione; SOD, superoxide dismutase; ALT, alanine aminotransferase; AST, aspartate aminotransferase; BUN, urea nitrogen; Cr, creatinine; CK, creatine kinase; TAG, triglyceride; TC, total cholesterol; ELISA, enzyme-linked immunosorbent assay; HRTEM, high-resolution TEM; OCT, optimal cutting temperature; Ti₃C₂Tx MXenes, titanium carbide MXene nanosheets; DAPI, 4′,6-diamidino-2-phenylindole; HO, hydroxyl free radical; PI, propidium iodide.

Data Sharing Statement

All data are available in the main text or the [Supplementary Materials](#). The raw sequencing data are available upon request.

Ethical Approval and Consent to Participate

Our project was approved by the Animal Ethics Committee of Guangzhou Medical University.

Acknowledgments

We thank Jingnan Qiu for administrative support.

Funding

This work was supported by the Basic Research Project of Peak Hospital (grant agreement no. 2023A03J0339 and 2025A03J4313) and the Plan on Enhancing Scientific Research in GMU (2024SRP062).

Disclosure

The authors report no conflicts of interest in this work.

References

1. Younossi ZM, Koenig AB, Abdelatif D, et al. Global epidemiology of nonalcoholic fatty liver disease-meta-analytic assessment of prevalence, incidence, and outcomes. *Hepatology*. **2016**;64:73–84. doi:10.1002/hep.28431
2. Wree A, Broderick L, Canbay A, Hoffman HM, Feldstein AE. From NAFLD to NASH to cirrhosis-new insights into disease mechanisms. *Nat Rev Gastroenterol Hepatol*. **2013**;10:627–636. doi:10.1038/nrgastro.2013.149
3. Zhao GN, Zhang P, Gong J, et al. Tmbim1 is a multivesicular body regulator that protects against non-alcoholic fatty liver disease in mice and monkeys by targeting the lysosomal degradation of Tlr4. *Nature Med*. **2017**;23(6):742–752. doi:10.1038/nm.4334
4. Neuschwander-Tetri BA. Non-alcoholic fatty liver disease. *BMC Med*. **2017**;15(45). doi:10.1186/s12916-017-0806-8
5. National Guideline Centre (UK). Non-alcoholic fatty liver disease: assessment and management. *NICE Guideline*. **2016**;10.
6. Clare K, Dillon JF, Brennan PN. Reactive oxygen species and oxidative stress in the pathogenesis of MAFLD. *J Clin Trans Hepatol*. **2022**;10:939–946. doi:10.14218/JCTH.2022.00067
7. Fang S, Wan X, Zou X, et al. Arsenic trioxide induces macrophage autophagy and atheroprotection by regulating ROS-dependent TFEB nuclear translocation and AKT/mTOR pathway. *Cell Death Dis*. **2021**;12:88.
8. Larabi A, Barnich N, Nguyen HTT. New insights into the interplay between autophagy, gut microbiota and inflammatory responses in IBD. *Autophagy*. **2019**;16:38–51. doi:10.1080/15548627.2019.1635384
9. Liu Z, Wang M, Wang X, et al. XBP1 deficiency promotes hepatocyte pyroptosis by impairing mitophagy to activate mtDNA-cGAS-STING signaling in macrophages during acute liver injury. *Redox Biol*. **2022**;52:102305. doi:10.1016/j.redox.2022.102305
10. Guillems M, Scott CL. Liver macrophages in health and disease. *Immunity*. **2022**;55:1515–1529. doi:10.1016/j.immuni.2022.08.002

11. Li X, Wang C, Cao Y, Wang G. Functional MXene materials: progress of their applications. *Chem Asian J.* 2018;13:2742–2757. doi:10.1002/asia.201800543
12. Lin H, Gao S, Dai C, Chen Y, Shi J. A two-dimensional biodegradable niobium carbide (MXene) for photothermal tumor eradication in NIR-I and NIR-II biowindows. *J Am Chem Soc.* 2017;139:16235–16247. doi:10.1021/jacs.7b07818
13. Wu Q, Li N, Wang Y, et al. A 2D transition metal carbide MXene-based SPR biosensor for ultrasensitive carcinoembryonic antigen detection. *Biosens Bioelectron.* 2019;144:111697. doi:10.1016/j.bios.2019.111697
14. Yin J, Pan S, Guo X, et al. Nb₂C mxene-functionalized scaffolds enables osteosarcoma phototherapy and angiogenesis/osteogenesis of bone defects. *Nanomicro Lett.* 2021;13:30. doi:10.1007/s40820-020-00547-6
15. Chuang Yang YL, Luo Y, Lin H, Ge M, Shi J, Zhang X. Niobium carbide mxene augmented medical implant elicits bacterial infection elimination and tissue regeneration. *ACS nano.* 2021;15:1086–1099. doi:10.1021/acsnano.0c08045
16. Ren J, Da J, Wu W, Zheng C, Hu N. Niobium carbide-mediated photothermal therapy for infected wound treatment. *Front Bioeng Biotechnol.* 2022;10:934981.
17. Yang Li RF, Fu R, Duan Z, Zhu C, Fan D. Artificial nonenzymatic antioxidant mxene nanosheet-anchored injectable hydrogel as a mild photothermal-controlled oxygen release platform for diabetic wound healing. *ACS nano.* 2022;16:7486–7502. doi:10.1021/acsnano.1c10575
18. Unal MA, Bayrakdar F, Fusco L, et al. 2D MXenes with antiviral and immunomodulatory properties: a pilot study against SARS-CoV-2. *Nano Today.* 2021;38:101136.
19. Zhang Z, Niu A, Lv Y, et al. NbC nanoparticles decorated carbon nanofibers as highly active and robust heterostructural electrocatalysts for ammonia synthesis. *Angew Chem Int Ed.* 2024;63.
20. Deng X, Zhang J, Qi K, et al. Ultrafast electron transfer at the In₂O₃/Nb₂O₅ S-scheme interface for CO₂ photoreduction. *Nat Commun.* 2024;15. doi:10.1038/s41467-024-49004-7
21. Valdecantos MP, Pardo V, Ruiz L, et al. A novel glucagon-like peptide 1/glucagon receptor dual agonist improves steatohepatitis and liver regeneration in mice. *Hepatology.* 2016.
22. Ma C, Kesarwala AH, Eggert T, et al. NAFLD causes selective CD4(+) T lymphocyte loss and promotes hepatocarcinogenesis. *Nature.* 2016;531:253–257. doi:10.1038/nature16969
23. Ye D, Yang K, Zang S, et al. Lipocalin-2 mediates non-alcoholic steatohepatitis by promoting neutrophil-macrophage crosstalk via the induction of CXCR2. *J Hepatol.* 2016;65:988–997. doi:10.1016/j.jhep.2016.05.041
24. Kleiner DE, Brunt EM, Van Natta M, et al. Design and validation of a histological scoring system for nonalcoholic fatty liver disease. *Hepatology.* 2005;41:1313–1321. doi:10.1002/hep.20701
25. Feng W, Han X, Hu H, et al. 2D vanadium carbide MXenzyme to alleviate ROSmediated inflammatory and neurodegenerative diseases. *Nat Commun.* 2021;12.
26. Jiang Z, Yuan B, Qiu N, et al. Manganese-zeolitic imidazolate frameworks-90 with high blood circulation stability for mri-guided tumor therapy. *Nano-Micro Lett.* 2019;11. doi:10.1007/s40820-019-0292-y
27. Eslam M, El-Serag HB, Francque S, et al. Metabolic (dysfunction)-associated fatty liver disease in individuals of normal weight. *Nat Rev Gastroenterol Hepatol.* 2022;19:638–651. doi:10.1038/s41575-022-00635-5
28. Eslam M, Sanyal AJ, George J, et al. MAFLD: a consensus-driven proposed nomenclature for metabolic associated fatty liver disease. *Gastroenterology.* 2020;158:1999–2014.
29. Carpino G, Del BM, Pastori D, et al. Increased liver localization of lipopolysaccharides in human and experimental non-alcoholic fatty liver disease. *Hepatology.* 2019.
30. Li T, Ma J, Wang W, Lei B. Bioactive MXene promoting angiogenesis and skeletal muscle regeneration through regulating M2 polarization and oxidation stress. *Adv Healthc Mater.* 2023;12.
31. Rafieerad A, Yan W, Alagarsamy KN, et al. Fabrication of Smart Tantalum Carbide MXene Quantum Dots with Intrinsic Immunomodulatory Properties for Treatment of Allograft Vasculopathy. *Adv Funct Mater.* 2021;31.
32. Van Welden S, Selfridge AC, Hindryckx P. Intestinal hypoxia and hypoxia-induced signalling as therapeutic targets for IBD. *Nat Rev Gastroenterol Hepatol.* 2017;14:596–611. doi:10.1038/nrgastro.2017.101
33. Kumar A, Sundaram K, Mu J, et al. High-fat diet-induced upregulation of exosomal phosphatidylcholine contributes to insulin resistance. *Nat Commun.* 2021;12:213. doi:10.1038/s41467-020-20500-w
34. Du X, Wu Z, Xu Y, et al. Increased Tim-3 expression alleviates liver injury by regulating macrophage activation in MCD-induced NASH mice. *Cell Mol Immunol.* 2018;16:878–886. doi:10.1038/s41423-018-0032-0
35. He S, Li J, Yao Z, et al. Insulin alleviates murine colitis through microbiome alterations and bile acid metabolism. *J Transl Med.* 2023;21. doi:10.1186/s12967-023-04214-3

International Journal of Nanomedicine

Publish your work in this journal

The International Journal of Nanomedicine is an international, peer-reviewed journal focusing on the application of nanotechnology in diagnostics, therapeutics, and drug delivery systems throughout the biomedical field. This journal is indexed on PubMed Central, MedLine, CAS, SciSearch®, Current Contents®/Clinical Medicine, Journal Citation Reports/Science Edition, EMBase, Scopus and the Elsevier Bibliographic databases. The manuscript management system is completely online and includes a very quick and fair peer-review system, which is all easy to use. Visit <http://www.dovepress.com/testimonials.php> to read real quotes from published authors.

Submit your manuscript here: <https://www.dovepress.com/international-journal-of-nanomedicine-journal>

Dovepress
Taylor & Francis Group